Letters

Automatic Resonance Tuning With ON/OFF Soft Switching for Push–Pull Parallel-Resonant Inverter in Wireless Power Transfer

Shahid Ali Khan and Dukju Ahn

***Abstract*—This letter proposes the tunable resonant tank and its control method for push–pull parallel-resonant inverter in wireless power transfer application. The parallel tuning capacitor is controlled using pulsewidth modulation, and its duty cycle is determined by the sensing of drain voltage waveshape. Soft switching is ensured at both the turn-ON and turn-OFF for every switches in the proposed inverter: zero voltage turn-ON and low *dv/dt* turn-OFF. The real-time tuning minimizes the voltage stress on switches and maximizes the output power, and guarantees soft switching regardless of detuning of parallel-resonant inverter. The voltage stress on the tunable element is lower than the stress on the main inverter part. Moreover, all the MOSFETs are connected to ground. Hence, the MOSFETs do not experience large resonant voltage swing across negative and positive levels. These also simplify the gate driving circuitry. The proposed tuning achieves higher efficiency than conventional switch-controlled capacitor due to the elimination of back-to-back two-series MOSFETs. The measurement verifies that the proposed method achieves maximum 1.96 times higher output power and 15.86% higher efficiency with the same voltage stress on switches.**

***Index Terms*—Push–pull parallel resonant inverter, variable capacitor, wireless power transfer.**

I. Introduction

MAXIMUM power transfer with high efficiency is critical in wireless power transfer. Among various wireless link topologies, current source parallel-resonant inverter has short-circuit protection and better performance under no load condition due to its current limiting dc-link characteristic [3]. Another advantages include less components, ease of implementation at high switching frequency [1], and a simple gate driving circuit [2]. Moreover, the output voltage is not a square wave but a sinusoid, which minimizes EMI harmonics.

In practical applications, self-inductance of TX is deviated from its nominal value due to various reasons. One of the reasons could be the distance variation between TX and RX coils because the metallic and shielding structure in RX affects the TX inductance. These cause detuning of resonant frequency, power fluctuations, high-voltage stress on switch, and low efficiency. Many researchers have used self-oscillating topologies [4]–[7] which automatically change the operating frequency, and ensure a constant load power and efficiency under distance variation. However, in many cases, usable frequency range is specified by government or industrial consortium agencies. For example, 85 kHz is commonly used for high-power application. Another example is 6.78 MHz ISM band. In these frequency bands, the frequency variation is not allowed. Moreover, some of EMI suppression techniques are tuned to a specified frequency because they use a tuned resonance circuit [8]–[10]. If the operating frequency is deviated, then the performance of those EMI suppression is degraded. In [11], an auxiliary resonant circuit is added between chopper and resonant inverter to achieve zero-voltage switching (ZVS). Even if [11] works well, low sampling delay of digital control can degrade the performance. In [12]–[13], the array of selectable switches and capacitors are bulky and costly. Kamineni *et al.* [14] proposed a mistuning-tolerant push–pull parallel-resonant inverter. It achieves soft switching only once among the turn-ON or turn-OFF transitions. Moreover, it requires additional diode in series with MOSFET switch. All these characteristics increase loss. Li *et al.* [15] proposed a tunable capacitor. Its drawbacks are that the switch experiences high-voltage stress across negative to positive levels because the switch is connected to the resonance node directly, and that the back-to-back MOSFET configuration causes twice loss.

Manuscript received January 13, 2022; revised March 11, 2022 and March 31, 2022; accepted April 17, 2022. Date of publication April 22, 2022; date of current version May 23, 2022. This work was supported in part by Incheon National University under Grant 2019-0416, and in part by National Research Foundation under Grant 2019R1F1A1063121. *(Corresponding author: Dukju Ahn.)*

The authors are with Incheon National University, Incheon 22012, South Korea (e-mail: sakciit@gmail.com; adjj22@gmail.com).

Color versions of one or more figures in this article are available at https://doi.org/10.1109/TPEL.2022.3168978.

Digital Object Identifier 10.1109/TPEL.2022.3168978

II. Problems of Conventional Techniques

A. Problems of Detuning in Push–Pull Inverter

Fig. 1(a) shows conventional current-fed parallel-resonant inverter. Fig. 1(b) shows the narrow pulsewidth and high peaking of V_{d1} due to smaller value of $C_{\mathrm{TX}} \times L_{\mathrm{TX}}$. This causes high-voltage stress on switches and degraded effective output voltage of inverter, all of which limits the output power of wireless link. On the other hand, if the L_{TX} is detuned to high value as in Fig. 1(c), the ZVS fails for M_1 and M_2, thus degrading efficiency. Therefore, to improve the output power, to reduce the voltage stress on switches, and to eliminate the ZVS losses, a real-time tuning is proposed.

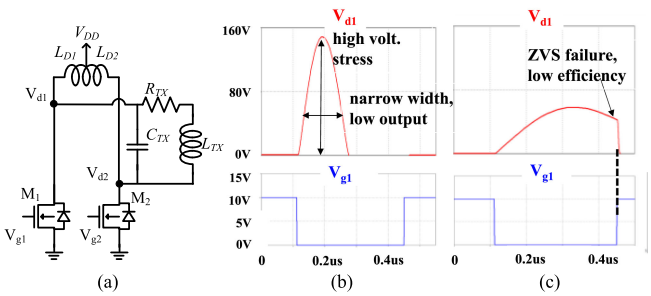

Fig. 1. Conventional push–pull parallel-resonant inverter. (a) Schematic. (b) When L_{TX} is detuned to low value. The effective output voltage of inverter is low, and the voltage stress on M_1 is high. (c) When L_{TX} is detuned to high value. The V_{d1} does not drop to zero before gate turns ON, which causes zero-voltage switching failure.

B. Drawbacks of Conventional Switch-Controlled Capacitor

The MOSFETs in conventional switch-controlled capacitors (SCCs) should be able to block the bidirectional resonant current. This requires two-series back-to-back MOSFETs, which cause twice loss [15]–[17]. Moreover, these MOSFETs experience high-voltage stress. The resonant voltage on these SCC is typically higher than the voltage of main inverter bridge. In addition, the source pin of MOSFET undergoes large ac voltage swing, which requires the photocoupled isolated gate driver and additional isolated power supply dedicated for the photocoupled gate driver.

Shui *et al.* [18] proposed another SCC topology. Their SCC contains both a capacitor and a ferrite-cored ac inductor, which partly cancel (resonate) out each other within an SCC. Therefore, the current at the SCC becomes higher than the current at the main coupling coil. This increases loss at the SCC.

Shi *et al.* [19] proposed an SCC in a full-bridge form. It experiences high-voltage stress as illustrated in [19]. Moreover, four switches are used, resulting in higher cost and loss.

In contrast, the loss in the proposed tuning is less than previous SCCs. This is because the proposed tuning does not need to block the bidirectional current, and therefore the two-series back-to-back configuration is not necessary.

In addition, the MOSFETs in proposed tuning experience less voltage stress. The voltage stress of proposed tuning is less than or equal to the voltage of main inverter. Moreover, the proposed circuit is referenced to ground, and therefore simplifies the gate driving.

III. Proposed Tuning Capacitor and Control Method

A. Proposed Switching Operations

Fig. 2(a) shows the proposed tuning inverter and its control loop. Waveforms of the proposed tuning are presented in Fig. 3. Fig. 4 shows the current flows. The C_{pwm1} and C_{pwm2} are the pulsewidth modulation (PWM) switched capacitors. The allowed region for the rising edge of V_{Gpwm1} is notated in the V_{Gpwm1} graph of Fig. 3. This is to guarantee the zero-voltage turn-ON of M_{pwm1}, as will be discussed in next section. Between t_2 and t_3, as the M_1 turns OFF, the I_{pwm1} starts to flow through C_{pwm1}. Even if the C_{pwm1} is connected at t_1, the I_{pwm1} does

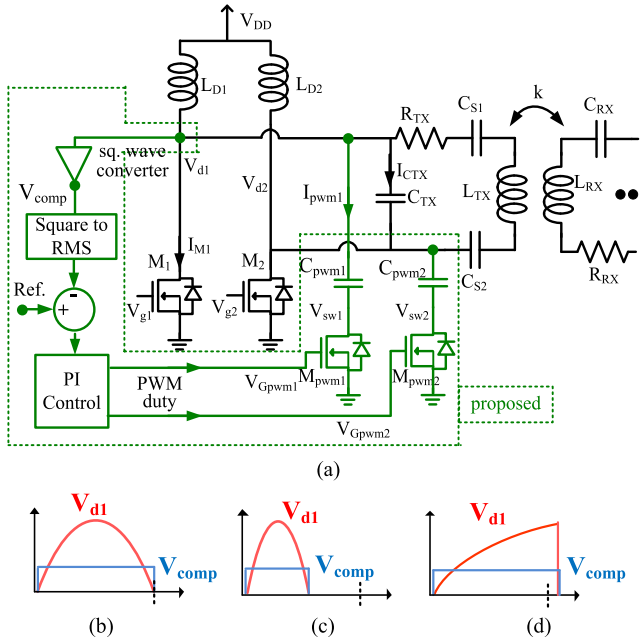

Fig. 2. Proposed tuning control for parallel-resonant inverter. (a) When M_{pwm1} is ON, L_{TX} resonates both with C_{TX} and C_{pwm1}. V_{d1} and comparator's output V_{comp}. (b) At perfect resonant condition. (c) When L_{TX} is detuned to a lower value. (d) When L_{TX} is detuned to higher value.

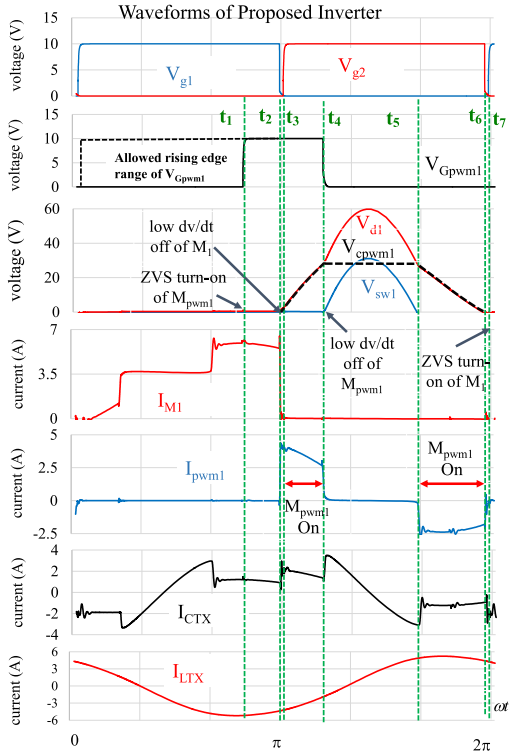

Fig. 3. Waveforms of the proposed autotuning inverter.

not flow when V_{g1} is high. At t_3–t_4, the slope of V_{d1} is slower because both the C_{pwm1} and C_{TX} are carrying resonant current. At t_4–t_5, the rate of change of V_{d1} is rapid because C_{pwm1} is OFF. At t_5–t_6, the V_{sw1} drops to zero and the diode of M_{pwm1} conducts. Therefore, the duty cycle of C_{pwm1} happens twice a

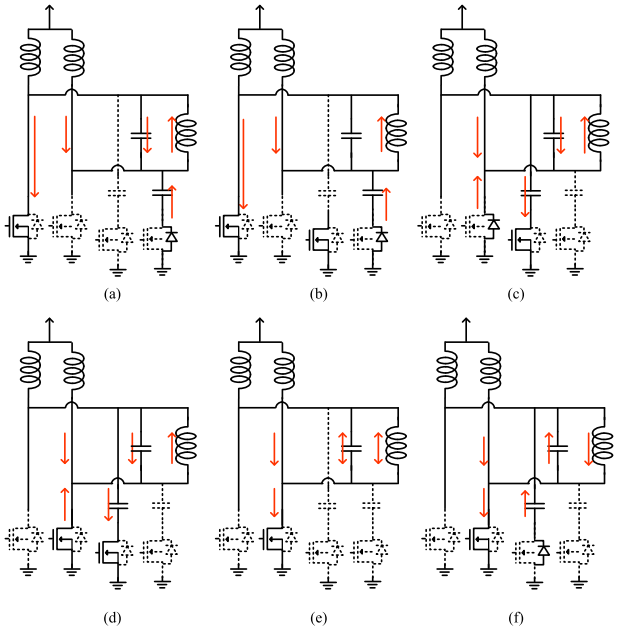

Fig. 4. Switching diagram of the proposed PWM tuning for current-fed resonant inverter. (a) Before t_1. (b) t_1–t_2. ZVS turning ON of M_{pwm1}, which does not conduct yet. (c) t_2–t_3, deadtime of V_{g1} and V_{g2}. I_{pwm1} and I_{CTX} start to conduct. V_{d1} rises. (d) t_3–t_4. I_{pwm1} keeps conducting. ZVS turning ON of M_2. (e) t_4–t_5. M_{pwm1} is OFF, I_{CTX} carries all of resonant current of L_{TX}. (f) t_5–t_6. V_{sw1} reaches zero, so M_{pwm1} (I_{pwm1}) conducts again.

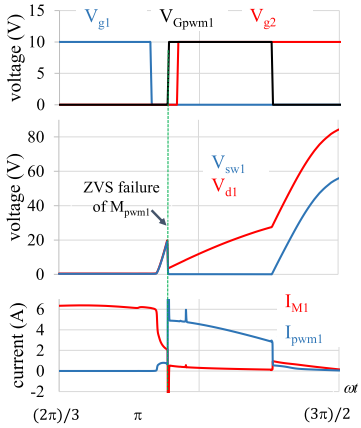

Fig. 5. ZVS fails for M_{pwm1} if V_{Gpwm1} is turned ON after the falling edge of V_{g1}.

period: t_3–t_4 and t_5–t_6. By adjusting the t_4 timing, the effective duty of C_{pwm1} is adjusted.

B. Zero-Vvoltage Turn-ON and Low dv/dt Turn-OFF

To ensure the zero-voltage turn-ON of M_{pwm1}, the rising edge of V_{Gpwm1} (t_1) must be aligned before the falling edge of V_{g1} referring to Fig. 3. This is because the V_{d1} and therefore V_{sw1} are 0 when V_{g1} is high. As shown in Fig. 5, if V_{Gpwm1} is turned ON after the falling edge of V_{g1}, ZVS fails for M_{pwm1}.

In Fig. 3, the turn-OFF of M_{pwm1} at t_4 is also soft- switching. The V_{sw1} does not rise abruptly (low *dv/dt*) at t_4. Therefore, the I_{pwm1} and V_{sw1} do not overlap and the switching loss is minimized.

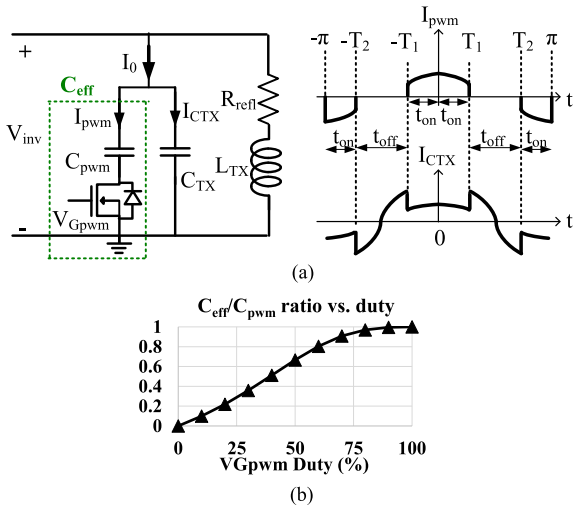

Fig. 6. (a) Equivalent circuit for effective capacitance calculation and waveforms. (b) $C_{\mathrm{eff}}/C_{\mathrm{pwm}}$ ratio with respect to duty cycle of V_{Gpwm}.

To guarantee zero-voltage turn-ON for M_1, the V_{d1} voltage should drop to zero before the rising edge of V_{g1} as in t_7. If the *LC* time constant is deviated to be large, it takes longer time for the V_{d1} to reach 0 V, and therefore ZVS fails as illustrated in Fig. 1(c). The proposed feedback loop monitors the waveshape of V_{d1} and accordingly adjusts the duty cycle of $V_{\mathrm{Gpwm(12)}}$ to guarantee ZVS of M_1 and M_2.

At the turn-OFF of M_1 (t_2), the drain voltage V_{d1} does not rise rapidly (low *dv/dt* OFF). This minimizes the overlap between voltage and current, thereby preventing switching losses.

To summarize, all the switches achieve soft switching at both turn-ON and turn-OFF.

C. Proposed Control

The strategy for maximizing output power and guaranteeing ZVS is that the V_{d1} voltage should avoid undesired waveforms such as Fig. 1(b) and (c). Fig. 1(b) has a problem of low output power and high-voltage stress. On the other hand, Fig. 1(c) fails ZVS, degrading efficiency. To detect the status of V_{d1}, the V_{d1} is sensed and its width is extracted, which is then inputted to microcontroller unit (MCU). Fig. 2(c) and (d) depicts that the extracted width of V_{d1} is narrow for condition shown in Fig. 1(b) and wide for condition of Fig. 1(c), compared to the perfect resonant condition shown in Fig. 2(b). The PI loop in MCU determines the turn-OFF time, t_4. Note that the t_5 is automatically set by t_4 because of symmetry of V_{sw1} waveform.

IV. Analysis of Duty Cycle and Effective Capacitance

As seen in Fig. 6(a), when C_{pwm} is turned ON, the resonant current divides into I_{CTX} and I_{pwm}. Currents I_{CTX} and I_{pwm} can be written as

$$I_{\mathrm{pwm}} = \begin{cases} \frac{I_0 C_{\mathrm{pwm}}}{C_{\mathrm{TX}}+C_{\mathrm{pwm}}} \cos(t), \text{for } 0 \le t \le T_1 \text{ and } T_2 \le t \le \pi \\ 0, \text{otherwise} \end{cases} \quad (1)$$

$$I_{\mathrm{CTX}} = \begin{cases} \frac{I_0 C_{\mathbf{TX}}}{C_{\mathbf{TX}}+C_{\mathrm{pwm}}} \cos(t) \text{ for } 0 \le t \le T_1 \text{ and } T_2 \le t \le \pi \\ I_0 \cos(t), \text{otherwise} \end{cases} \tag{2}$$

where I_0 is the amplitude of summation of I_{CTX} and I_{pwm} which is in cosine form. The fundamental element of I_{pwm} and $I_{\mathrm{pwm\_Fund}}$ can be obtained using Fourier series as follows:

$$\begin{aligned} I_{\mathrm{pwm\_Fund}} &= \frac{2}{\pi}\int_0^{T1} \frac{I_0 C_{\mathrm{pwm}}}{C_{\mathbf{TX}}+C_{\mathrm{pwm}}} \cos t \cos t dt \\ &\quad + \frac{2}{\pi}\int_{T2}^{\pi} \frac{I_0 C_{\mathrm{pwm}}}{C_{\mathbf{TX}}+C_{\mathrm{pwm}}} \cos t \cos t dt \\ &= \frac{I_0 C_{\mathrm{pwm}}}{\pi\,(C_{\mathbf{TX}}+C_{\mathrm{pwm}})} \left(\frac{\sin 2T_1 - \sin 2T_2}{2} + T_1 - T_2 + \pi \right). \end{aligned} \tag{3}$$

Similarly, the fundamental element of I_{CTX} is calculated as

$$\begin{aligned} I_{\mathrm{CTX\_Fund}} &= \frac{I_0 C_{\mathrm{TX}}}{\pi\,(C_{\mathbf{TX}}+C_{\mathrm{pwm}})} \\ &\quad \times \left(\frac{\sin 2T_1 - \sin 2T_2}{2} + T_1 - T_2 + \pi \right) \\ &\quad + \frac{I_0}{\pi} \left(\frac{\sin 2T_2 - \sin 2T_1}{2} - T_1 + T_2 \right). \end{aligned} \tag{4}$$

Referring to Fig. 6(a), C_{eff} is the effective capacitance of the duty-controlled C_{pwm}. The voltage across C_{TX} and C_{eff} are the same with each other because they are at the same V_{inv} node. Their voltages are written as

$$\frac{I_{\mathrm{CTX}}}{j\omega C_{\mathbf{TX}}} = \frac{I_{\mathrm{pwm}}}{j\omega C_{\mathrm{eff}}} = V_{\mathrm{inv}}. \tag{5}$$

Substituting (3) and (4) into (5) gives, (6) shown at the bottom of this page,

Fig. 6(b) shows the effective capacitance ratio of $C_{\mathrm{eff}}/C_{\mathrm{pwm}}$ as a function of duty cycle.

V. Measurement Results

Fig. 7(a) presents the experimental setup which is comprised of current-fed push–pull resonant inverter, TX and RX coils, RX rectifier, sensor board, and TMS320F28335 as MCU. The detuning of L_{TX} with respect to TX-to-RX distance is presented in Fig. 7(b). The coil diameter is 15 cm. The operating frequency is a fixed 85 kHz which is suitable for small-sized devices.

In Figs. 8 and 9, the "conventional" refers to inverter with fixed resonant capacitance. Figs. 8(a) and 9(a) show that the effective output voltage, V_{d1}, is small because the V_{d1} does not occupy the full region where the V_{g1} is zero. V_{d1}'s pulsewidth is less than 70%. At TX–RX distance of 6 cm, conventional system can output only 132.5 W compared to the proposed system which outputs 200 W.

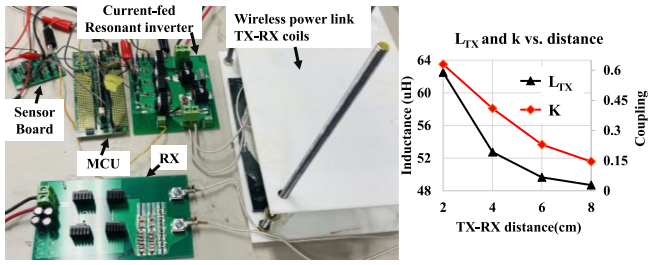

Fig. 7. Experimental setup. (a) TX inverter, RX rectifier, sensor, and MCU boards. (b) Variation of L_{TX} and coupling k with respect to TX–RX distance.

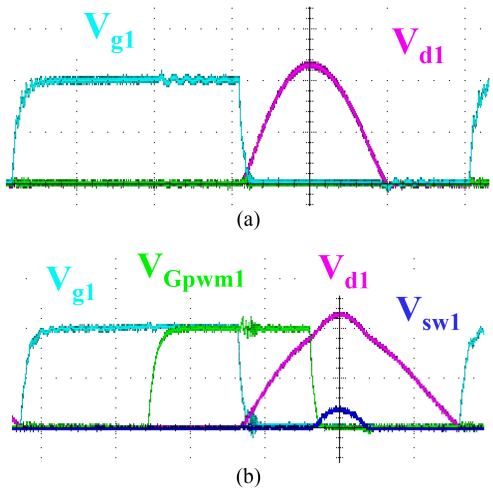

Fig. 8. Waveform comparison between conventional and proposed. TX–RX distance is set to 6 cm (V_{d1}: 50 V/div, V_{g1}: 5 V/div, V_{Gmpwm1}: 5 v/div, and time: 2.00 μs /div). With the same maximum voltage limit on V_{d1}, the available output power is improved. (a) Conventional without tuning. RX power is limited to 132.5 W due to the narrow inverter voltage of V_{d1}. (b) Proposed with tuning. RX power is improved to 200 W.

Fig. 10 shows the waveform of I_{CPWM1} which is similar with Fig. 3. The operation of C_{PWM2} and C_{PWM1} are identical but has phase difference of 180°. Both C_{PWM2} and C_{PWM1} are controlled by a single PI controller, and have the same duty cycle for a specific TX–RX distance.

Dynamic tuning of the proposed system is presented in Fig. 11. In this setup, the TX–RX distance is abruptly changed from 8 to 6 cm. The dc component of blue waveform represents the rms value of V_{comp} which is the sensed waveshape of V_{d1}. In response to the rise of rms value of V_{comp} due to distance change, the PI controller reduces the duty of C_{pwm1} and C_{pwm2} to maintain a constant V_{comp}.

Fig. 12(a) presents the improvement in RX received power at different RX distances. The voltage stress on switch is regulated to be identical between conventional and proposed for comparison purpose. At TX–RX distance of 8 cm, the received power is doubled at proposed inverter. Fig. 12(b) compares the

$$C_{\mathrm{eff}} = \frac{\frac{C_{\mathrm{TX}} C_{\mathrm{pwm}}}{(C_{\mathbf{TX}}+C_{\mathrm{pwm}})} \left(\frac{\sin 2T_1 - \sin 2T_2}{2} + T_1 - T_2 + \pi \right)}{\frac{C_{\mathrm{TX}}}{(C_{\mathbf{TX}}+C_{\mathrm{pwm}})} \left(\frac{\sin 2T_1 - \sin 2T_2}{2} + T_1 - T_2 + \pi \right) + \left(\frac{\sin 2T_2 - \sin 2T_1}{2} - T_1 + T_2 \right)} \tag{6}$$

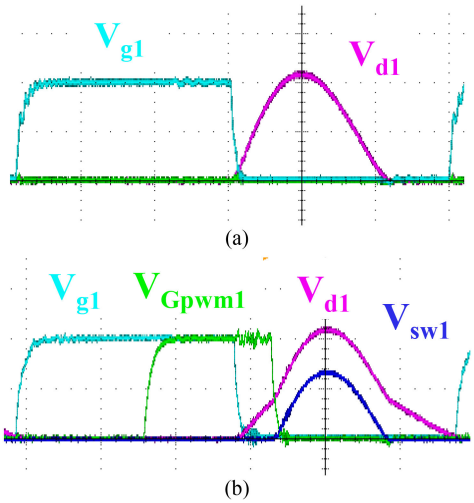

Fig. 9. TX–RX distance is set to 4 cm (V_{d1}: 50 V/div, V_{g1}: 5 V/div, V_{Gmpwm1}: 5 v/div, and time: 2.00 μs/div). (a) Conventional without tuning. RX power is limited to 181.02 W. (b) Proposed with tuning. RX power is improved to 200 W.

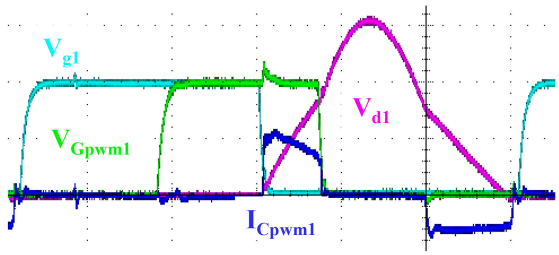

Fig. 10. V_{Gpwm1} should be turned ON before the falling edge of V_{g1} to ensure ZVS. I_{Cpwm1} starts to flow as V_{g1} turns OFF (V_{d1}: 50 V/div, V_{g1}: 5 V/div, V_{Gpwm1}: 5 V/div, I_{Cpwm1}: 4 A/div, and time: 2.00 μs/div).

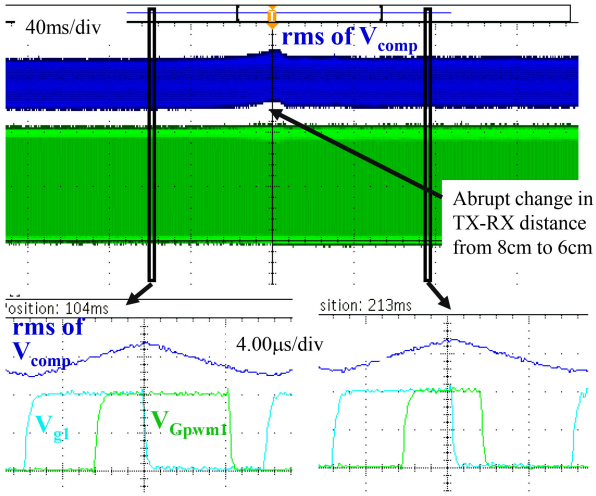

Fig. 11. Dynamic tuning of the proposed control system (V_{comp}: 500 mV/div, V_{g1}: 5 V/div, and V_{Gpwm1}: 5 V/div).

TX-to-RX efficiency between the systems with and without the proposed tuning. For the conventional case of black square curve in Fig. 12(b), efficiency drops when TX–RX distance is short due to the failure of ZVS caused by detuning of L_{TX}, which is as illustrated in Fig. 1(c). Fig. 12(c) and (d) shows the loss

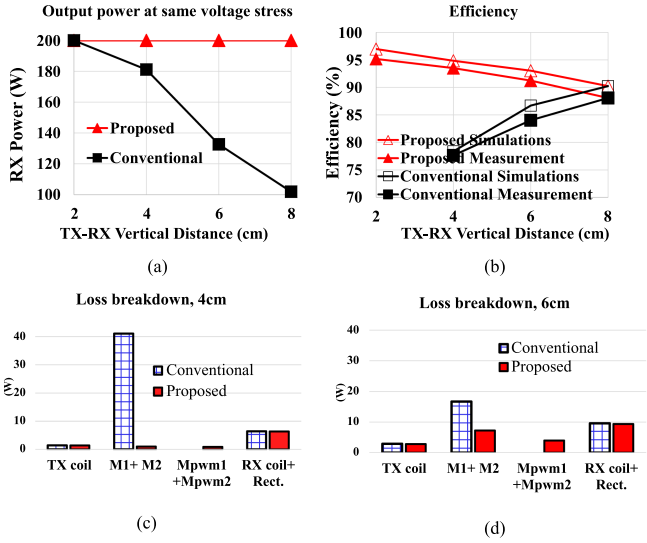

Fig. 12. RX power and TX-to-RX efficiency comparison between the conventional and the proposed method. (a) RX power with respect to distance. (b) TX-to-RX efficiency with respect to distance. (c) Loss break down at TX-RX distance of 4 cm. (d) Loss break down at TX–RX distance of 6 cm.

TABLE I
COMPARISON AT THE SAME 200 W LOAD AND COIL PARAMETERS

WORKS	MAX. VOLTAGE STRESS (V_{DS})	MOSFET SOURCE PIN VOLTAGE RANGE	LOSS FROM TUNING MOSFET	NECESSITY OF ISOLATED GATE SUPPLY
[16]	248V	-247~21V	7.7W	Yes
[17]	442V	-442~48V	5.58W	Yes
[18]	419V	-420~340V	11.4W	Yes
[19]	157V	-550~554V	5.08W	Yes
This paper	110V	0V	4.1W	No

breakdown analysis of proposed and conventional. In conventional system, decreasing TX–RX distance causes ZVS failure, resulting in high switching losses of M_1+M_2. Table I shows the comparison between the proposed and the conventional SCC. The load power, coil parameters, coupling, and semiconductor devices are kept identical for comparison purpose. Our proposed method provides the lowest loss and voltage stress at tuning MOSFET at the same load power and coil parameters.

VI. CONCLUSION

A duty-cycle-controlled tuning capacitor for push–pull parallel-resonant inverter and its control method are proposed. This reduces the voltage stress on the switches of inverter and improves the output power. All the MOSFETs in the main inverter and in the tuning part achieve soft switching both at turn-ON and turn-OFF: zero-voltage turn-ON and low dv/dt turn-OFF for all switches. The MOSFET's source node is connected to ground, which simplifies the gate driving circuitry. The voltage stress on the tuning MOSFET is less than the stress on the main inverter part. These are another advantages compared to previous tuning topologies which experience high resonance voltage swing across negative to positive levels.

REFERENCES

[1] H. Kobayashi, J. M. Hinrichs, and P. M. Asbeck, "Current-mode class-D power amplifiers for high-efficiency RF applications," *IEEE Trans. Microw. Theory Techn.*, vol. 49, no. 12, pp. 2480–2485, Dec. 2001.

[2] M. K. Kazimierczuk and D. Czarkowski, *Resonant Power Converters*. New York, NY, USA: Wiley, 1995.

[3] S. Chudjuarjeen, C. Koompai, and V. Monyakul, "Full-bridge current-fed inverter with automatic frequency control for forging application," in *Proc. IEEE Region 10 Conf. TENCON*, 2004, pp. 128–131.

[4] A. Namadmalan and J. Moghani, "Tunable self-oscillating switching technique for current source induction heating systems," *IEEE Trans. Power Electron.*, vol. 61, no. 5, pp. 2556–2563, May 2014.

[5] A. Abdolkhani and A. Hu, "Improved autonomous current-fed push-pull resonant inverter," *IET Power Electron.*, vol. 7, no. 8, pp. 2103–2110, Aug. 2014.

[6] D. Ahn and S. Hong, "Wireless power transmission with self-regulated output voltage for biomedical implant," *IEEE Trans. Ind. Electron.*, vol. 61, no. 5, pp. 2225–2235, May 2014.

[7] A. Namadmalan, "Self-oscillating pulsewidth modulation for inductive power transfer systems," *IEEE J. Emerg. Sel. Topics Power Electron.*, vol. 8, no. 2, pp. 1813–1820, Jun. 2020.

[8] S. Hong *et al.*, "A frequency-selective EMI reduction method for tightly coupled wireless power transfer systems using resonant frequency control of a shielding coil in smartphone application," *IEEE Trans. Electromagn. Compat.*, vol. 61, no. 6, pp. 2031–2039, Dec. 2019.

[9] J. Kim and S. Ahn, "Dual loop reactive shield application of wireless power transfer system for leakage magnetic field reduction and efficiency enhancement," *IEEE Access*, vol. 9, pp. 118307–118323, 2021.

[10] J. Park *et al.*, "A resonant reactive shielding for planar wireless power transfer system in smartphone application," *IEEE Trans. Electromagn. Compat.*, vol. 59, no. 2, pp. 695–703, Apr. 2017.

[11] Z. Wang, Y. Xu, P. Liu, Y. Zhang, and J. He, "Zero-voltage-switching current source inverter fed PMSM drives with reduced EMI," *IEEE Trans. Power Electron.*, vol. 36, no. 1, pp. 761–771, Jan. 2021.

[12] D. Siemaszko, C. Rod, and A. C. Rufer, "Single-phase resonant *LC* circuit using a bank of self-switched capacitors," *IEEE Trans. Ind. Electron.*, vol. 58, no. 9, pp. 4175–4184, Sep. 2011.

[13] A. Kamineni, G. Covic, and J. Boys, "Self-tuning power supply for inductive charging," *IEEE Trans. Power Electron.*, vol. 32, no. 5, pp. 3467–3479, May 2017.

[14] A. Kamineni, M. Neath, G. Covic, and J. Boys, "A mistuning-tolerant and controllable power supply for roadway wireless power systems," *IEEE Trans. Power Electron.*, vol. 32, no. 9, pp. 6689–6699, Sep. 2017.

[15] W. Li, G. Wei, C. Cui, X. Zhang, and Q. Zhang, "A double-side self-tuning LCC/S system using a variable switched capacitor based on parameter recognition," *IEEE Trans. Ind. Electron.*, vol. 68, no. 4, pp. 3069–3078, Apr. 2021.

[16] J. Zhang, J. Zhao, Y. Zhang, and F. Deng, "A wireless power transfer system with dual switch-controlled capacitors for efficiency optimization," *IEEE Trans. Power Electron.*, vol. 35, no. 6, pp. 6091–6101, Jun. 2020.

[17] H. Zhang, Y. Chen, C.-H. Jo, S.-J. Park, and D.-H. Kim, "DC-link and switched capacitor control for varying coupling conditions in inductive power transfer system for unmanned aerial vehicles," *IEEE Trans. Power Electron.*, vol. 36, no. 5, pp. 5108–5120, May 2021.

[18] H. Shui, D. Yu, S. Yu, H. Iu, T. Fernando, and H. Cheng, "An autonomous impedance adaptation strategy for wireless power transfer system using phase-controlled switched capacitors," *IEEE J. Emerg. Sel. Topics Power Electron.*, vol. 9, no. 2, pp. 2303–2316, Apr. 2021.

[19] L. Shi, P. Alou, J. Oliver, J. Rodriguez, A. Delgado, and J. Cobos, "A self-adaptive wireless power transfer system to cancel the reactance," *IEEE Trans. Ind. Electron.*, vol. 68, no. 12, pp. 12141–12151, Dec. 2021.